RSC Advances

PAPER

View Article Online
View Journal | View Issue

Cite this: *RSC Adv.*, 2024, **14**, 10199

Nonlinear optical and spectroscopic properties, thermal analysis, and hemolytic capacity evaluation of quinoline-1,3-benzodioxole chalcone†

Efraín Polo-Cuadrado,[a] Edison Osorio,[b] Karen Acosta-Quiroga,[c] Paola Andrea Camargo-Ayala,[d] Iván Brito,[e] Jany Rodriguez,[f] Joel B. Alderete,[g] Oscar Forero-Doria,[h] Edgard Fabián Blanco-Acuña*[i] and Margarita Gutiérrez*[j]

This article describes the synthesis, characterization (^{1}H NMR, ^{13}C NMR, FT-IR, HRMS and XRD), UV-Vis absorption and fluorescence spectra, theoretical analysis, evaluation of nonlinear optical properties (NLO), thermal analysis and determination of the hemolytic capacity of the compound (*E*)-*N*-(4-(3-(benzo[*d*][1,3]dioxol-5-yl)acryloyl)phenyl)quinoline-3-carboxamide (**5**). Radiological findings showed that compound **5** crystallized in space group $Pca2_1$. Furthermore, theoretical DFT studies performed with the B3LYP and M062X functionals showed good agreement with the experimental results and provided valuable information on the molecular and electronic structure, reactivity, polarizability, and kinematic stability of the compound. Besides, compound **5** did not show any hemolytic effect on human erythrocytes and exhibited strong NLO properties. The TG and DTA thermograms of quinoline–chalcone (**5**) revealed a multi-step thermal decomposition process with a total mass loss of 83.2%, including water content loss. The DTA curves exhibited endothermic peaks corresponding to decomposition steps, melting point, and thermochemical transition. Additionally, exothermic peaks in the DTA thermograms align with significant mass loss, confirming the compound's melting point and water content, as validated by X-ray diffraction analysis. These results contribute to the advancement of research on compounds with NLO properties and offer a promising avenue for the development of substances potentially applicable to optical devices in the biomedical field.

Received 1st February 2024
Accepted 21st March 2024

DOI: 10.1039/d4ra00820k

rsc.li/rsc-advances

1. Introduction

Nonlinear optics (NLO) is a field of study that explores the interaction between light and matter when the polarization response is nonlinear with respect to the electric field. The study of NLO characteristics, such as the nonlinear refractive index, nonlinear absorption coefficient, and NLO susceptibility, has become more significant in recent years owing to the development of photonic and optoelectronic devices. These materials are widely used in optical computing, optical switching, optical data storage, optical limiting, up conversion lasers, biomedicine, microscopy, among others.[1,2]

A NLO material experimentally exhibits a nonlinear optical phenomenon, which corresponds to the conversion of light wavelength, amplification of light and conversion of refractive index as a function of optical intensity. In the search for new materials, the study of first and second polarizability values allows researchers to predict and optimize materials for specific NLO applications. A non-zero first polarizability (α) indicates that the material can be polarized by an electric field, which is a prerequisite for NLO effects to occur; and a non-zero second polarizability (β) value determines the strength and type of NLO

[a]*Depto. Química Orgánica, Fac. Ciencias Químicas, Universidad de Concepción, Chile*
[b]*Facultad de Ciencias Naturales y Matemáticas, Universidad de Ibagué, Carrera 22 Calle 67, Ibagué 730001, Colombia*
[c]*Departamento de Química Orgánica y Fisicoquímica, Doctorado en Química, Universidad de Chile, Santiago, Chile*
[d]*Departamento de Ciencias Básicas Biomédicas, Facultad de Ciencias de la Salud, Universidad de Talca, Talca, Chile*
[e]*Departamento de Química, Facultad de Ciencias Básicas, Universidad de Antofagasta, Avda, Campus Coloso, Antofagasta 02800, Chile*
[f]*Doctorado en Ciencias Mención I + D de Productos Bioactivos, Instituto de Química de Recursos Naturales, Universidad de Talca, Casilla 747, Talca 3460000, Chile*
[g]*Instituto de Química de Recursos Naturales (IQRN), Universidad de Talca, Avenida Lircay S/N, Casilla 747, Talca, Chile*
[h]*Departamento de Ciencias Básicas, Facultad de Ciencias, Universidad Santo Tomás, Talca 3460000, Chile*
[i]*Grupo de Investigación en Ciencias Básicas (NÚCLEO), Facultad de Ciencias e Ingeniería, Universidad de Boyacá, 150003, Tunja, Boyacá, Colombia. E-mail: efblanco@uniboyaca.edu.co*
[j]*Laboratorio Síntesis Orgánica y Actividad Biológica (LSO-Act-Bio), Instituto de Química de Recursos Naturales, Universidad de Talca, Casilla 747, Talca 3460000, Chile. E-mail: mgutierrez@utalca.cl*

† Electronic supplementary information (ESI) available. CCDC 2299694. For ESI and crystallographic data in CIF or other electronic format see DOI: https://doi.org/10.1039/d4ra00820k

effect, reflecting the nonlinear response of the material to the applied electric field.[3]

An example of an NLO phenomenon is second harmonic generation (SHG), in which two photons of the same frequency are combined to generate a new photon at twice the original frequency. SHG has been widely studied for its unique optical properties, which supply valuable information about the underlying physics and the materials involved in this process. Over the years, researchers have made noteworthy progress in understanding and improving SHG, finding that organic molecules are a promising source of potent SHG materials because their structures can be tuned to achieve the desired NLO properties. In addition, chromophoric organic compounds can delocalize the electronic charge distribution, which leads to high mobility due to the overlap of π orbitals, giving them great NLO properties.[1,4]

Chalcones are a class of chromophoric organic compounds with several characteristics that make them suitable candidates for strong SHG generation.[4–9] These features include extended π-conjugation, non-centrosymmetric structure, enhanced nonlinear optical response, structural flexibility, and nonlinear wave mixing capabilities (see Fig. 1). In general, it has been proved that chalcones are a class of organic compounds that usually exhibit satisfactory NLO properties, with enormous potential in the design of optical devices, comparable and even superior to urea.[4,6] On the other hand, it has been understood that second-order molecular nonlinearity in chalcones can be enhanced by large delocalized π-electron systems with strong electron donor and acceptor groups.[4,5]

The basic strategy of including electron donor and acceptor substituents to polarize the π-electron system of organic materials has been employed in the development of NLO chromophores with high first and second order hyperpolarizabilities, good thermal stability, improved solubility and processability.[8,10]

In addition to what was previously mentioned, chalcones with biologically relevant groups such as quinolines or 1,3-benzodioxol derivatives stand out for their wide variety of biological properties, such as antioxidants, antimicrobials, anticancer, anti-inflammatory, among others.[11–17] These properties, together with their intrinsic NLO properties, make chalcones especially interesting for the design of optical materials with biomedical applications. However, it is essential to take into account that, due to the special care required by materials that come into contact with biological tissue, it is important that the candidate compounds do not present toxicological characteristics, including the induction of hemolysis, which is the rupture of the red blood cells in the blood, and can have harmful effects on the body.[18]

For this reason, in the present work the synthesis and characterization of the chalcone quinoline-1,3-benzodioxole (**5**) is presented by means of infrared (IR) spectroscopy, proton (^{1}H NMR) and carbon (^{13}C NMR) nuclear magnetic resonance, high resolution mass spectrometry (HRMS) and single crystal X-ray diffraction (XRD). Likewise, the absorption and emission behavior, thermal stability (TG/DTA) and the hemolytic effect on human erythrocytes are studied. Theoretical DFT calculations are used to gain more knowledge regarding the electronic and molecular structure, as well as the NLO properties, given the important potential of **5** in the development of optical devices applicable to the biomedical field. It is important to note that the results presented for compound **5** are derived from theoretical calculations and are compared with other compounds known to exhibit NLO properties, as direct experimental data are not available. This comparison is made to provide a preliminary assessment of its potential NLO behavior.

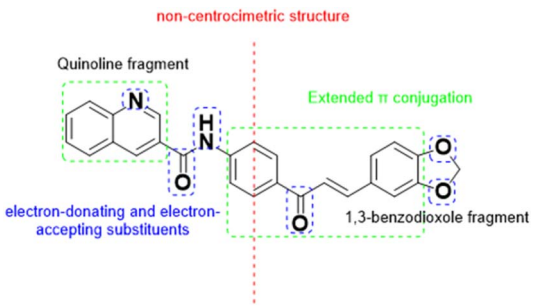

Fig. 1 Typical characteristics that confer and improve NLO properties to chalcones.

2. Experimental

2.1. Materials and methods

All chemical reagents and organic solvents were obtained from commercial suppliers and used without further purification. Thin-layer chromatography (TLC) was performed to check the purity of compounds on silica gel 60 HF254 plates (Merck, Germany). The melting point ranges (m.p.) were taken on an Electrothermal IA9100 apparatus (Stone, UK) using the one-end open capillary method and were uncorrected. IR spectra (KBr discs, 500–4000 cm^{-1}) were recorded on a NEXUS 670 FT-IR spectrophotometer (Thermo Nicolet, USA). ^{1}H and ^{13}C NMR spectra were recorded using DMSO-d_6 and $CDCl_3$ as solvents and tetramethylsilane (TMS) as an internal reference on an AM-400 spectrometer (Bruker, Germany) at working frequencies 400 and 100 MHz, respectively. High resolution mass spectrometry (HRMS) analyses were conducted using a Bruker "Compact" quadrupole time-of-flight mass spectrometry (qTOF-MS, Germany) coupled with an Apollo II ion funnel electrospray ionization (ESI) source. UV-Vis absorption and fluorescence spectra were recorded in methanol at 10 μM using UV/Visible Metertech SP-8001 and Hitachi F-2710 spectrophotometers, respectively. In both cases, cells with an optical path of 10 mm were used and the fluorescence was acquired with a slit width of 2.5 nm.

2.2. Synthesis *N*-(4-acetylphenyl)quinoline-3-carboxamide (3)

Quinoline derivative (**1**) was prepared according to our previously reported experimental procedure (Scheme 1).[19] A mixture of commercial quinoline-3-carboxylic acid and freshly distilled

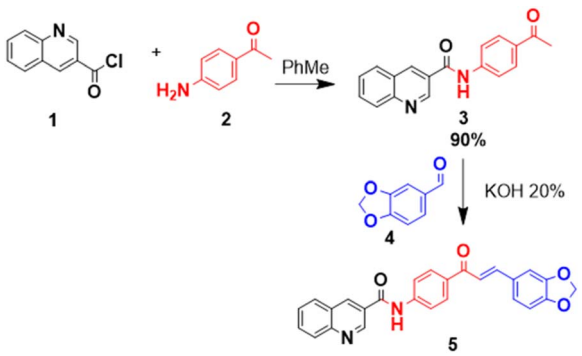

Scheme 1 Synthesis of quinoline-1,3-benzodioxole chalcone **5**.

thionyl chloride was warmed into reflux for 3 h, then cooled to room temperature and evaporated under vacuum to dryness to quantitatively obtain the corresponding chloride acids (**1**). This crude material was used without further purification. A mixture of this acyl chloride (**1**, 1.0 equiv.) and 4-aminoacetophenone (**2**, 1.0 equiv.) in toluene (10 mL) was stirred at room temperature for 2 h and then treated with a saturated $NaHCO_3$ solution. The biphasic solution was vigorously stirred for 30 min, then decanted, and finally separated. The collected aqueous phase was extracted with EtOAc (2 × 10 mL). The combined organic layer was dried over Na_2SO_4 and evaporated. The solid was washed with icy water and crude material was crystallized from ethanol. Yield 90%, white solid; m.p. = 255–257 °C; IR (KBr, cm^{-1}): 3327, 3068, 3001, 1985, 1918, 1844, 1676, 1650, 1597, 1268, 1109, 799; ^{1}H NMR (400 MHz, DMSO-d_6) δ_H (ppm): 2.55 (s, 3H), 7.71 (t, J = 8.0 Hz, 1H), 7.89 (t, J = 8.0 Hz, 1H), 7.99 (s, 4H), 8.12 (dd, J = 8.0, 12.3 Hz, 2H), 8.99 (s, 1H), 9.37 (s, 1H), 10.90 (bs, 1H); ^{13}C NMR (100 MHz, DMSO-d_6) δ_C (ppm): 26.4 (CH_3), 119.5 (2 × CH), 126.3 (C), 127.3 (C), 127.5 (CH), 128.8 (CH), 129.2 (CH), 129.3 (2 × CH), 131.5 (CH), 132.2 (C), 136.2 (CH), 143.4 (C), 148.5 (C), 149.0 (CH), 164.5 (C), 196.5 (C).

2.3. Synthesis and crystallization of (*E*)-*N*-(4-(3-(benzo[*d*][1,3]dioxol-5-yl)acryloyl)phenyl)quinoline-3-carboxamide (5)

The quinolone-1,3-benzodioxole chalcone derivative **5** was prepared according to our previously reported experimental procedure (Scheme 1).[20] A solution of equimolar amounts of piperonal (**4**) (1 mmol) and ketone (**3**) (1 mmol) was placed in an Erlenmeyer flask together with 20% potassium hydroxide (0.5 mL) and absolute ethanol (10 mL). This mixture was sonicated at room temperature for an appropriate time (10–20 min) until the reaction was completed (the reaction was monitored by TLC). The reaction mixture was then treated with a cold bath and filtered to leave a solid product, which was washed with a hexane, followed by recrystallization from ethanol to obtain the desired compound. Yield 92% (388.6 mg); yellow solid; m.p. = 237–239 °C; IR (KBr, cm^{-1}): 3334, 2917, 1670, 1595, 1528, 1499, 1534, 1245, 1025, 920, 819, 755; ^{1}H NMR (400 MHz, DMSO-d_6) δ_H (ppm): 6.10 (s, 2H), 6.99 (d, J = 7.8 Hz, 1H), 7.33 (d, J = 8.1 Hz, 1H), 7.66 (s, 1H), 7.69–7.72 (m, 2H), 7.83 (s, 1H), 7.88–7.90 (m, 1H), 8.01 (d, J = 8.6 Hz, 2H), 8.13 (dd, J = 8.3, 16.1 Hz, 2H), 8.21 (d, J = 8.6 Hz, 2H), 9.00 (s, 1H), 9.39 (s, 1H), 10.93 (bs, 1H); ^{13}C NMR (100 MHz, DMSO-d_6) δ_C (ppm): 102.0 (CH_2), 107.3 (CH), 108.9 (CH), 120.7 (CH), 121.7 (CH), 125.9 (CH), 127.3 (C), 127.4 (CH), 129.1 (2 × CH), 129.5 (2 × CH), 130.0 (2 × CH), 130.9 (CH), 135.9 (CH), 143.0 (CH), 148.5 (C), 148.6 (C), 149.7 (C), 150.8 (C), 165.9 (C), 187.4 (C); HRMS (ESI, m/z): calculated for $C_{26}H_{19}N_2O_4$ $[M + H]^+$ 423.1345; found 423.1342.

2.4. X-ray crystal structure determination

Suitable crystals of the chalcone derivative **5** were chosen for the X-ray crystallographic analysis. X-ray intensity data were collected at 296 K in a Bruker D8 Venture diffractometer equipped with a bidimensional CMOS Photon 100 detector, using Mo-Kα radiation of wavelength 0.71073 Å. The diffraction frames were integrated using the APEX3 package and were corrected for absorption effects using the multi-scan method (SADABS). The crystal structure was solved by intrinsic phasing using the OLEX2 program.[21] Refinement was conducted by full-matrix least-squares methods based on F2 (SHELXL-2014).[22] Figures of the X-ray structure of the title compound were generated with the help of OLEX2 and ORTEP program packages. Crystallographic information files were deposited in the Cambridge Crystallographic Data Centre (CCDC) with the deposition number 2299694.†

2.5. Hemolytic assay

To rapidly assess the cellular toxicity of compound **5**, we used a percent hemolysis assay.[23] Briefly, non-heparinized blood was collected from a healthy volunteer type O Rh (+). Red blood cells were washed 3 times in PBS (10 mM sodium phosphate buffered saline, 150 mM sodium chloride pH 7.8 ± 0.2), and then diluted with PBS to obtain a 10% suspension. Compound **5** was dissolved in 400 μM DMSO and then PBS was added to prepare 10 serial dilutions starting from 200 μM to 0.39 μM using a microplate, each dilution was mixed 1 : 1 with the red blood cell solution for one volume final 200 μL per well, subsequently mixed gently and incubated at 37 °C with periodic pressure for 60 min of incubation. The solution was then centrifuged at 3000 rpm for 5 min. The absorbance of the supernatant was measured at 540 nm using an Epoch™ microplate photometer (BioTek® Instruments, Inc. Winooski, Vermont 05404-0998 USA). Finally, the hemolytic % was calculated by comparison with 100% of the hemolytic activity caused by Tween 20 as maximum hemolytic control. The hemolytic percentage developed by the PBS control and (1%, w/v) DMSO was used as negative control and blank for the readings in all groups. Each experiment was performed in triplicate at all concentrations used.

The hemolytic % was calculated with the formula:

$$\text{Hemolytic}(\%) = \frac{\text{ODt} - \text{ODnc}}{\text{ODpc} - \text{ODnc}} \times 100\%$$

where ODt is the absorbance of each dilution of the analyzed compound, ODpc is the absorbance of the positive control and ODnc is the absorbance of the negative control.

2.6. Thermal analysis

Thermogravimetry (TG) and differential thermal analysis (DTA) of quinoline–chalcone (**5**) was registered on a thermogravimetric analyzer TGA-Q500 (TA Instruments, New Castle, DE, USA) using a nitrogen atmosphere from room temperature to 800 °C and a heating rate of 5 °C min^{-1}, with a flow rate of 60 mL min^{-1}. Also, 40 mL min^{-1} of N_2 was used as protection gas into the electronic balance; 5.67 mg of **5** was placed into a Pt crucible for each analysis.

3. Computational methods

3.1. Theoretical calculations

The X-ray diffraction experimental result of the title compound was directly taken for an initial molecular geometry. The geometry optimization of the monomeric structure was conducted using the M062X functional and 6-311++G(d,p) basis set in the gas phase.[24,25] M062X is a hybrid meta exchange–correlation functional with double the nonlocal exchange (2X), which is parametrized for nonmetal and long noncovalent range interactions.[26] The theoretical UV-Vis electronic spectrum and optimization of the geometry of the first excited state (S_1) of the monomeric structure were performed through the time-dependent density-functional theory (TDDFT) calculations at the M062X/6-311++G(d,p) level.[27,28] The solvent effect of methanol on the calculated electronic properties of the studied compound was implemented using the polarizable continuum model (PCM).[29]

Density functional theory (DFT) was employed to optimize the ground-state geometries and compute the vibrational frequencies of compound **5**. These calculations were performed with the B3LYP functional and the 6-31G(d) basis set,[30–34] since this level of calculation provides a good description of electronic correlations, and exchange interactions. In addition, it is computationally more cost-effective and works quite well to theoretically simulate IR spectra. The calculated vibrational frequencies were scaled by 0.960.[35]

The frontier molecular orbitals (FMOs), the highest occupied molecular orbital (HOMO) and lowest unoccupied molecular orbital (LUMO), which account for the ability to donate and accept electrons, respectively, were calculated at M062X/6-311++G(d,p) level.[36] Some global reactivity descriptors, such as HOMO–LUMO gap, chemical hardness (η), chemical potential (μ), electrophilicity index (ω), and chemical softness (S), which are based on the HOMO and LUMO energies were studied to measure the stability of the synthesized compound. Chemcraft (**https://www.chemcraftprog.com**) and GaussView 6.0 (ref. 37) programs were used to draw structures and molecular graphs, likewise, all calculations were performed using Gaussian 09 software.[37]

3.2. NLO properties

The electric dipole moment, linear polarizability, and the first and second hyperpolarizability tensors were evaluated using finite field (FF) approach to explore the non-lineal optical (NLO) properties of the compound **5** with a field frequency of 0.0010 au at the CAM-B3LYP/6-311G++(d,p) level.

DFT functional has shown results close to CCSD and MP2 methodologies,[38,39] showing efficiency and accuracy for calculation of second order hyperpolarizability. In the FF method, when a molecule is subjected to a static field (F), the energy (E) of the molecule can be expressed as:

$$E = E^0 - \mu_i F_i - \frac{1}{2}\alpha_{ij}F_iF_j - \frac{1}{6}\beta_{ijk}F_iF_jF_k - \frac{1}{24}\gamma_{ijkl}F_iF_jF_kF_l - \ldots$$

Where E^0 is the energy of the molecule in the absence of an electric field. μ corresponds to the average dipole moment vector and it is given as:

$$\mu = (\mu_x{}^2 + \mu_y{}^2 + \mu_z{}^2)^{1/2}$$

Afterwards, the static or linear polarizability (α_0) and total polarizability $\Delta(\alpha)$ tensors can be defined as follows

$$\alpha_0 = \frac{1}{3}(\alpha_{xx} + \alpha_{yy} + \alpha_{zz})$$

$$\Delta\alpha = \frac{1}{\sqrt{2}}\sqrt{(\alpha_{xx} - \alpha_{yy})^2 + (\alpha_{yy} - \alpha_{zz})^2 + (\alpha_{zz} - \alpha_{xx})^2 + 6\alpha_{xz}{}^2}$$

Following the main equation, the first hyperpolarizability β can be calculated using the following equations:

$$\beta_i = \beta_{iii} + \sum_{i \neq j}\left[\frac{\beta_{ijj} + 2\beta_{jii}}{3}\right]$$

So, the magnitude of first hyperpolarizability (β_{tot}) can be calculated by following equation.

$$\beta_{tot} = \sqrt{(\beta_x{}^2 + \beta_y{}^2 + \beta_z{}^2)}$$

where

$$\begin{aligned}\beta_x &= (\beta_{xxx} + \beta_{xxy} + \beta_{xyy})\\ \beta_y &= (\beta_{yyy} + \beta_{xxz} + \beta_{yyz})\\ \beta_z &= (\beta_{xzz} + \beta_{yzz} + \beta_{zzz})\end{aligned}$$

Therefore

$$\begin{aligned}\beta_{tot} = [&(\beta_{xxx} + \beta_{xxy} + \beta_{xyy})^2 + (\beta_{yyy} + \beta_{xxz} + \beta_{yyz})^2\\ &+ (\beta_{xzz} + \beta_{yzz} + \beta_{zzz})^2]^{1/2}\end{aligned}$$

and β_0 was also calculated by the following relation:

$$\beta_0 = \beta_{tot} \times \frac{3}{5}$$

Finally, the average second hyperpolarizability tensors γ, will be describe as follows:

$$\langle\gamma\rangle = \frac{1}{5}[\gamma_{xxxx} + \gamma_{yyyy} + \gamma_{zzzz} + 2[\gamma_{xxyy} + \gamma_{yyzz} + \gamma_{xxzz}]]$$

All equations have been taken from reported published by Abbas *et al.*[40]

4. Results and discussion

4.1. Chemistry and characterization

Fig. S1† and Table 1 show the results of the experimental and simulated infrared (IR) spectra for the molecule **5** using the B3LYP/6-31G(d) method. Table 1 lists the resulting vibration frequencies for the optimized geometries, the proposed vibration assignments, and the IR intensities, in decreasing order. Comparisons of theoretical and experimental IR spectra show that strong vibrations in the experimental spectrum are also strong in the theoretical spectrum.

On the other hand, Table 1 shows some valuable IR frequencies to find critical functional groups in the molecule **5**, which contribute to its characterization. N–H stretching of the amide residue in the molecule is seen in the range of 3334 cm^{-1}, and gaps are also saw at 3008 and 2917 cm^{-1}, which belong to the C–H sp^2 and C–H sp^3 stretches, respectively. Furthermore, at 1670 cm^{-1} it can be seen the C=O stretching band that corresponds to the ketone and amide groups superimposed on the same band. Meanwhile, at 1595 and 1354 cm^{-1} the bands corresponding to the C=C stretching and the C–H rolling in the plane appear. Furthermore, at 1670 cm^{-1}, the C=O stretching band corresponding to ketone and amide groups can be observed, overlapping in the same region. Meanwhile, bands at 1595 and 1354 cm^{-1} represent the C=C stretching and C–H (sp^3) rocking in the plane, respectively. Finally, at 1245 cm^{-1}, the band corresponding to the C–O–C stretching of the 1,3-benzodioxole moiety in the structure is observed, and this is the most intense band in both the theoretical and experimental spectra. As shown in Table 1, the frequencies calculated with the B3LYP/6-31G(d) method showed a good affinity with the results obtained experimentally. Therefore, this computational method is valuable in showing important functional groups for characterizing the molecules studied here.[41]

4.2. Hemolysis assay

The hemolytic assay was performed with PBS 1× as negative control (pH = 7.0) and Tween 20 as 100% hemolysis causing positive control. Equal amounts of RBCs (red blood cells) suspended in varying concentrations (0.2–100 μM) of ligand displayed <5% hemolysis, which is an acceptable standard (see Scheme 2). The results of this assay are significant as they indicate that chalcone **5** does not have a hemolytic effect on human erythrocytes. Hemolysis is a process that can be detrimental to human health, as it can release hemoglobin into circulation, which, in turn, can lead to the formation of blood clots and other health issues.[42] Therefore, the lack of a hemolytic effect of chalcone is an important and promising finding.

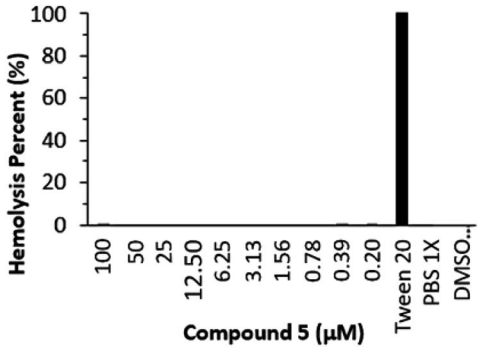

Scheme 2 Hemolytic effect of compound **5** (0.2–100 μM) on human erythrocytes.

However, it is important to note that the absence of a hemolytic effect on human erythrocytes is not necessarily indicative of the overall safety of chalcone in all contexts. Other potential effects of chalcone on different cell types or tissues need to be more thoroughly investigated. Additionally, it is crucial to consider that biological safety is only one of many factors to consider when evaluating a substance for use in pharmaceutical or therapeutic applications.

4.3. X-ray single crystal studies

The compound **5** crystallizes in space group $Pca2_1$. There are two water molecules and two independent organic molecules in the asymmetric unit, which slightly differs in their molecular conformation, Fig. 2.

Both molecules are just planar, maximum r.m.s deviation 0.095 Å and have an *E* conformation about the exocyclic C=C bond. The torsion is C8–C10–N2–C11/C8A–C10A–N2A–C11A are 178.7(3) and 177.3 for each molecule, respectively (178(3)° mean).

Table 1 Comparison of calculated and experimental vibration spectra (FTIR) of compound **5**

B3LYP/6-31G(d)			Experimental in this study	
Normal mode	Freq (cm^{-1})	Intensity (km mol^{-1})	Freq (cm^{-1})	Approximate assignments
1	3468	0.03	3334	N–H stretching
2	3019	0.09	3008	Asymmetric stretching C–H sp^2 (phenyl)
3	2924	0.37	2917	Symmetric stretching C–H sp^3
5	1697 and 1671	0.39 and 0.21	1670	Stretching C=O ketone and amide
6	1584	0.94	1595	Stretching C=C
8	1395	0.55	1354	Rocking in the C–H (sp^3) plane
9	1256	1	1245	C–O–C stretch

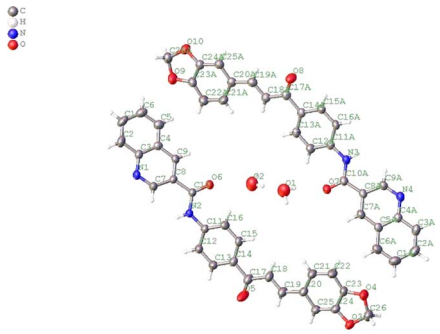

Fig. 2 ORTEP view of the title compound drawn at 30% of probability thermal displacement ellipsoids.

In the crystal, the molecules are anti-parallel to each other and run down the *a*-axis and are linked by two kind of hydrogen bond interaction: OW–H···O (carbonyl group), H5···O2 2.20, C5···O2 3.22(5) Å, C–H···O 129°; H···N 2.474(5) Å, N···N 3.297(4) Å, N–H···N 162(5)°; H···N 2.456(5) Å, C···N 3.362(4) Å, C–H···N 165(11)°, forming chains and no-centrosymmetric ring with graph-set notation S(8) and R_1^2, respectively (Bersntein), forming a three dimensional network (see Fig. 3). The crystal packing is further connected to another *via* weak π–π stacking interaction between benzene rings C1/C2/C3/C4/C5/C6; C1A/C2A/C3A/C4A/C5A/C6A with centroid–centroid distances of 3.724 and 3.779 Å, respectively (see Fig. 4). (Cg–Cgi; CgA–CgAii, symmetry code: (i) $x-1+y, z$; (ii) $x+1+y, z$.)

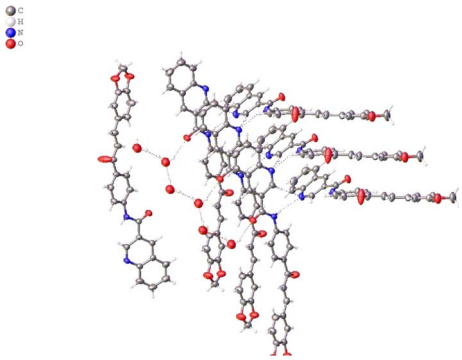

Fig. 3 Hydrogen bond interactions of the title compound. Some hydrogen atoms were omitted for clarity.

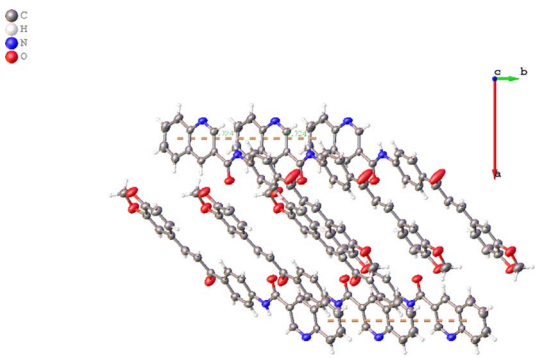

Fig. 4 π–π interactions in compound **5**.

4.4. Comparison of geometry data

A distances comparative analysis between experimental and theoretical chemical bonds are presented in Fig. 5. The root mean squared (RMS) value predicted by Chemcraft software, which accounts for the difference between the monomer from X-ray diffraction experiment and the theoretically optimized geometry, was low: 0.266 Å. Then, a good agreement was found between the optimized molecular geometrical parameters and experimental ones. As expected, the molecular geometry is practically flat, which favors conjugation and intramolecular electron transfer in the ground state (S_0). Likewise, an intramolecular interaction is observed between the C=O group of the amide and the *ortho* hydrogens of the phenyl moiety, which would favor the coplanarity of the amide-quinoline fragment with the α,β-unsaturated system.

4.5. Optical properties

4.5.1. Absorption spectrum. The comparison of the experimental and theoretical UV-Vis spectra of the title compound has been studied. The experimental spectrum scanned in methanol solution within the range of 190–450 nm includes two principal bands localized around 316 and 365 nm (Fig. 6a). Taking into account the cross-conjugation in the amide group, it is inferred that the maximum at 316 nm corresponds to a π → π* electronic transition of the quinoline fragment. Similarly, the maximum at 365 nm is consistent with a π → π* electronic transition of the system α,β-unsaturated (chalcone). In this sense, the bands below 250 nm correspond to n → σ* and π → σ* electronic transitions. This is in agreement with the absorption spectra of quinoline and chalcone phenyl-1,3-benzodioxole moieties reported in the literature.[43,44] The theoretical electronic spectrum (see Fig. 6b) matches the experimental UV-Vis spectrum. The transitions to the first 15 singlet excited states were calculated. Table 2 presents the main electronic transitions (except for $S_0 \rightarrow S_1$, transitions with $f < 0.2$ have been omitted). The $S_0 \rightarrow S_1$ transition at 341.17 nm has a very small oscillator strength ($f = 0.0060$). Consequently, the $S_0 \rightarrow S_2$ transition at 335.55 nm with a high $f = 1.1410$ and with a HOMO–LUMO contribution of 77% is correlated with the experimental absorption maximum at 365 nm. The second band located at 288.63 nm with $f = 0.7703$ arises from an $S_0 \rightarrow S_3$ transition with the main HOMO−1–LUMO contribution of

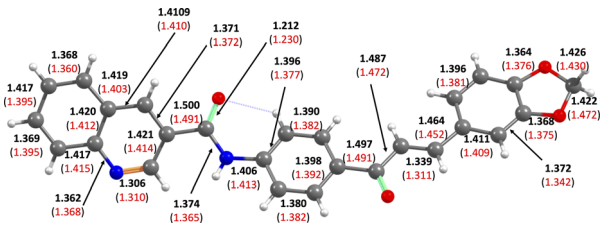

Fig. 5 Chemical bond distances scheme (in Angstrom). The values in brackets correspond to experimental data.

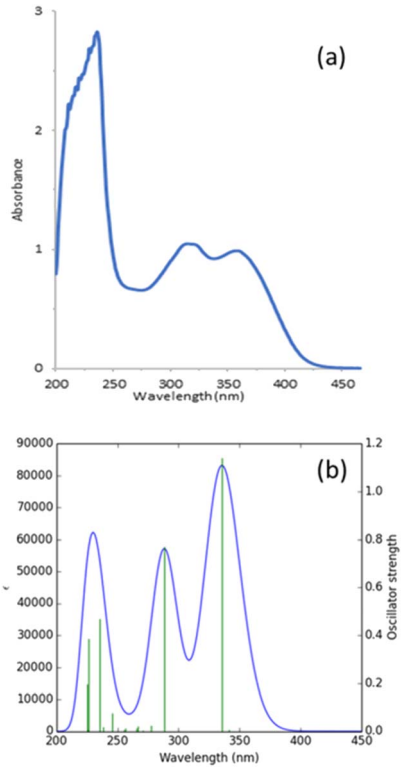

Fig. 6 Experimental (a) and calculated (b) electronic absorption spectra of title compound in methanol.

79%, which is consistent with the experimental band at 316 nm. Additionally, the broad band between 200 and 250 nm in the experimental spectrum would correspond mainly to $S_0 \rightarrow S_{12}$ (235.22 nm) and $S_0 \rightarrow S_{13}$ (226.43 nm) transitions. As can also be seen in Fig. 6, the theoretical spectrum only presents values greater than 219 nm. Those values lower than this wavelength could not be simulated in our TDDFT calculations.

4.5.2. Fluorescence spectrum. The experimental spectrum of fluorescence in methanol at different excitation wavelengths is presented in Fig. 7. After exciting compound 5 in the three bands of maximum absorption, the same emission spectrum was obtained with a maximum λ at 513 nm, but with different emissive intensities. This indicates that when excited at 360 nm a greater number of molecules emit radiative energy, most likely from the same excited state of lower energy S_1. Furthermore, it is observed that compound **5** shows a high Stokes shift of 148 nm (7904.08 cm^{-1}). It should be noted that the protic polar

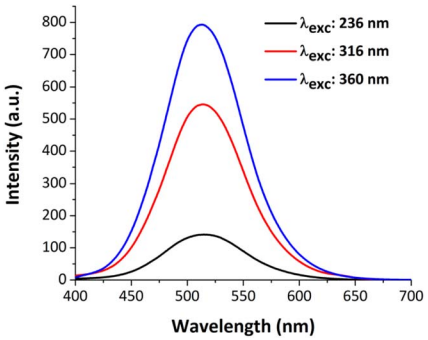

Fig. 7 Fluorescence spectra of compound **5** in methanol at different excitation wavelengths (λ_{exc}).

solvent does not generate a complete quenching of the fluorescence due to some intermolecular hydrogen bond interaction with compound **5**.

To gain more insight into the excited state, the geometry of the first excited state S_1 was optimized with the same level of ground state theory, but using the TDDFT formalism. Fig. 8 shows the optimized geometry of state S_1, where at first glance no significant change in the geometry is observed with respect to state S_0. However, Table 3 presents the geometric parameters that showed changes between each state. It is noteworthy that the changes in bond lengths and angles are mainly in the fragment of the α,β-unsaturated system, indicating that the fluorescent emission occurs from a locally excited state. Additionally, the variation of the C11–C13–C14–C19 dihedral angle indicates that the amide group tends to align with the plane of the α,β-unsaturated system so that the nitrogen donates electron density towards the electron-withdrawing carbonyl group. Beyond what was mentioned, the geometric parameters of compound **5** are not significantly altered after excitation.

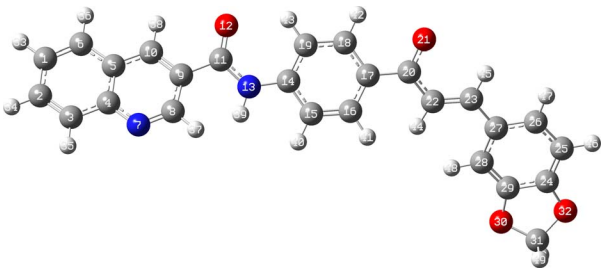

Fig. 8 Optimized geometry of the excited state S_1 in the gas phase.

Table 2 Main electronic transitions calculated in MeOH of compound **5**

Excited state	Excitation vertical (nm)	E_{cal}[a] (eV)	f_{os}[b]	Major contribution (%)
S_1	341.17	3.6341	0.0060	H−6 → L+0 (48%)
S_2	335.55	3.6949	1.1410	H+0 → L+0 (77%)
S_3	288.63	4.2957	0.7703	H−1 → L+0 (79%)
S_{12}	235.22	5.2709	0.4695	H+0 → L+2 (20%)
S_{13}	226.43	5.4757	0.3844	H−1 → L+2 (12%)

[a] Calculated transition energy. [b] Oscillator strength. H: HOMO, L: LUMO.

Table 3 Representative bond lengths (Å) and angles (°) of the optimized geometries of compound **5** in the S_0 and S_1 states

Bond	State S_0	State S_1
C20–O21	1.215	1.290
C20–C22	1.487	1.425
C22–C23	1.339	1.361
C23–C27	1.464	1.455
C17–C20	1.497	1.471
Angle		
C20–C22–C23	119.50	124.21
C17–C20–C21	120.02	116.18
C21–C20–C22	121.30	119.62
C18–C17–C20–O21	12.87	20.69
O21–C20–C22–C23	6.09	5.00
C11–C13–C14–C19	7.40	2.61

4.6. Frontier molecular orbitals (FMOs) analysis and molecular reactivity

The frontier molecular orbitals (FMOs), HOMO and LUMO, are the main orbitals responsible for chemical stability or reactivity. The HOMO–LUMO plots for the title compound is shown in Fig. 9. The molecular form of the HOMO shows a high electron density located mainly in the α,β-unsaturated-1,3-benzodioxole fragment, without encompassing the quinoline-amide group. On the other hand, in the LUMO the regions with the highest electronic probability are observed in the quinoline-amide residue together with the α,β-unsaturated ketone. The above indicates that there is a good intramolecular charge transfer (ICT) from the main donor group 1,3-benzodioxole towards the acceptor α,β-unsaturated carbonyl moiety. This good ICT is extremely favorable for the NLO properties of compound **5**.

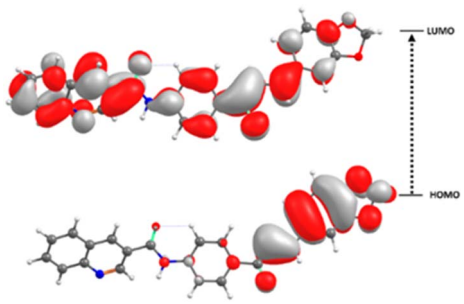

Fig. 9 HOMO and LUMO frontier molecular orbitals of **5**.

HOMO energy is associated with the electron-donating ability of a compound, while LUMO energy with electron accepting. The FMO energy gap supplies information about chemical reactivity and kinetic stability. A molecule with a small frontier orbital gap is associated with a high chemical reactivity and low kinetic stability. The HOMO and LUMO energies, and frontier orbital energy gap of the title compound were found to be −7.3259, −1.6120, and 5.7138 eV, respectively. The calculated values of the chemical hardness, chemical potential, electrophilicity index, and chemical softness parameters for the compound described above are 2.86, −4.47, 3.50 eV, and 0.18 eV^{-1}, respectively. The 1,3-benzodioxole chalcone derivative is expected to be less polarizable and associated with a low chemical reactivity due to its larger molecular gap and chemical hardness values, saying a hard molecule with low polarizability with high kinetic stability.

4.7. Nonlinear optical (NLO) properties

The dipole moment, polarizability and hyperpolarizability results obtained at CAM-B3LYP/6-311++g(d,p) level of theory is presented in Table 4. Urea as well as two published compounds with NLO properties have been used as prototype molecules for a comparative approach to NLO properties.

The relevance of polarizability and hyperpolarizability of a molecular system depends on electronic communication between two distinct parts of a molecule. The results showed non-zero μ values for the title compound, which should cause microscopic quadratic and cubic hyperpolarizabilities, with resulting non-zero values derived by the second numerical derivatives of electric dipole moments to the field implemented (see Table 4). Although dipole moment for compound **5** is lower than comparative molecules, the linear polarizability tensor α is the highest value reported in Table 4. It quantifies how the electron distribution within the material can be distorted or shifted when subjected to an external electric field. The high first and second hyperpolarizability (β and γ, respectively) values presented by compound **5** are indicative that the material shows strong NLO effects. This is crucial for advanced NLO applications, such as all-optical signal processing, optical switching, and the development of highly efficient NLO devices.

4.8. Thermal analysis studied

The Fig. 10 shows both TG and DTA thermograms of quinoline–chalcone **5**, recorded from room temperature to 800 °C, the thermal decomposition processes occurred as several

Table 4 Dipole moment, polarizability and hyperpolarizability values obtained at CAM-B3LYP/6-311++g(d,p) level of theory

Substance	μ (D)	α_0 ($\times 10^{-24}$ esu)	$\Delta\alpha$ ($\times 10^{-24}$ esu)	β_{tot} ($\times 10^{-30}$ esu)	β_0 ($\times 10^{-30}$ esu)	γ ($\times 10^{-36}$ esu)
Studied compound **5**	2.911	56.250	49.839	30.909	18.546	212.464
Urea	3.875	4.823	1.964	0.768	0.461	2.941
(*E*)-1-(1,3-Benzodioxol-5-yl)-4,4-dimethylpent-1-en-3-one[45]	3.546	27.625	21.645	21.550	12.930	44.189
(2*E*)-1-(1,3-Benzodioxol-5-yl)-3-phenylprop-2-en-1-one (SSP1)[46]	3.011	31.346	31.145	5.398	3.239	67.879

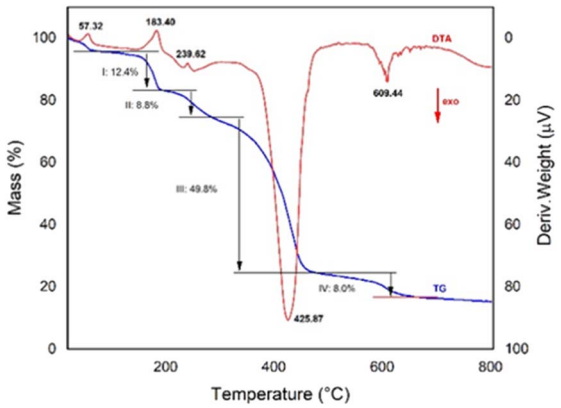

Fig. 10 TG-DTA thermograms of quinoline–chalcone **5**.

consecutive and simultaneous steps of mass loss, mainly four steps with a total mass loss of 83.2% considering a loss water content of 4.2 wt%. The four steps of mass loss were observed in the temperature range from 68.7 to 656.7 °C and mass loss values of 12.37, 8.8, 49.8 and 8.0%, respectively. The DTA curves reveals a succession of endothermic peaks located at 57.32, 183.40 and 239.62 °C, these endothermic peaks match with the decomposition I and II steps of TG curve and which are attributable to thermochemical transition and melting point, respectively.

Furthermore, in the region of 317 to 672 °C of DTA thermograms are observed two exothermic peaks at 425.87 and 609.44 °C, which are found inside the greatest mass loss of 49.8% (step III) with the maximum degradation temperature (T_m/°C) of 425.87 °C, accompanied by a minor mass loss of 8.0% (step IV) with a T_m/°C of 609.44 °C.

In summary, the TG/DTA analysis corroborated the melting point (Fusiometer measurement m.p.: 237–239 °C; m.p. from DTA curve: 239.62 °C) of the chalcone **5**, thus as confirmed the presence of 4.2 wt% water content that contrasts with the molecular formula ($C_{26}H_{19}N_2O_4 \cdot H_2O$) confirmed by diffraction X-rays analysis.

5. Conclusions

In this study, the quinoline-1,3-benzodioxole chalcone **5** was synthesized and characterized. Crystallographic studies showed that compound **5** crystallized in the $Pca2_1$ space group, with two water molecules and two independent organic molecules in the asymmetric unit. Both molecules are planar, with a maximum rms deviation of 0.095 Å, and have an *E* conformation concerning the C=C exocyclic bond.

Theoretical studies showed good agreement with experimental data from infrared (IR) and ultraviolet-visible (UV-Vis) spectroscopy. Experimentally, chalcone **5** showed three absorption maxima in the ultraviolet region, while the fluorescent emission originated from a locally excited state, since DFT calculations did not yield significant changes in the geometry of the S_0 and S_1 states. Furthermore, based on the chemical descriptors obtained by DFT analysis, the chalcone **5** is expected to be a hard molecule with low polarizability and high kinetic stability.

The TG and DTA thermograms of compound **5** revealed a multi-step thermal decomposition process with a total mass loss of 83.2%, including the loss of water content. The DTA curves exhibit endothermic peaks corresponding to decomposition steps, melting point, and thermochemical transition. Additionally, exothermic peaks in the DTA thermograms align with significant mass loss, confirming the melting point and water content of the compound, as validated by X-ray diffraction analysis.

Hemolysis assay showed that chalcone **5** had no effect on human erythrocytes. The absence of hemolysis, together with the strong NLO properties of the compound, make it a promising substance for the design of highly efficient optical devices with potential applications in biomedicine.

Although our work provides great insight into the synthesis, characterization, and potential applications of chalcone **5**, there are still many avenues for future research. First, given the theoretical promise of the nonlinear optical (NLO) properties of chalcone **5**, further experiments are required to determine its potential in this context. Additionally, investigating structural modification of chalcone **5** to improve NLO activity or tailor its properties to specific applications could be a fruitful area of research. Additionally, since the compound lacks hemolytic activity and potential biomedical applications, future studies may further examine its biological activity and therapeutic potential, including *in vitro* and *in vivo* studies to evaluate its efficacy and safety.

Conflicts of interest

There are no conflicts to declare.

Acknowledgements

The authors acknowledge the Research Group of the Laboratory of Organic Synthesis and Biological Activity of the University of Talca. Fondecyt Projects 1200531, and 3220681. The authors also acknowledge to FONDEQUIP program (EQM 130021, 160063 and 180024). This work was supported by the Universidad de Ibagué Research Fund, Ibague, Colombia, project No. 20-002-INT.

References

1 N. Sudha, R. Surendran and S. Jeyaram, *Opt. Mater.*, 2022, **131**, 112668.
2 N. V. Agrinskaya, V. A. Lukoshkin, V. V. Kudryavtsev, G. I. Nosova, N. A. Solovskaya and A. V. Yakimanskiĭ, *Phys. Solid State*, 1999, **41**, 1914–1917.
3 R. Bano, M. Asghar, K. Ayub, T. Mahmood, J. Iqbal, S. Tabassum, R. Zakaria and M. A. Gilani, *Front. Mater.*, 2021, **8**, 783239.
4 S. Omar, M. Shkir, M. Ajmal Khan, Z. Ahmad and S. AlFaify, *Optik*, 2020, **204**, 164172.

5 H. Belahlou, S. Abed, M. Bouchouit, S. Taboukhat, L. Messaadia, E. E. Bendeif, A. Bouraiou, B. Sahraoui and K. Bouchouit, *J. Mol. Struct.*, 2023, **1294**, 136488.
6 A. Saha, V. Shukla, S. Choudhury and J. Jayabalan, *Chem. Phys. Lett.*, 2016, **653**, 184–189.
7 L. R. Almeida, M. M. Anjos, G. C. Ribeiro, C. Valverde, D. F. S. Machado, G. R. Oliveira, H. B. Napolitano and H. C. B. De Oliveira, *New J. Chem.*, 2017, **41**, 1744–1754.
8 B. Ganapayya, A. Jayarama and S. M. Dharmaprakash, *Mol. Cryst. Liq. Cryst.*, 2013, **571**, 87–98.
9 P. J. Tejkiran, M. S. Brahma Teja, P. Sai Siva Kumar, P. Sankar, R. Philip, S. Naveen, N. K. Lokanath and G. Nageswara Rao, *J. Photochem. Photobiol., A*, 2016, **324**, 33–39.
10 E. F. Blanco-Acuña, L. A. Vázquez-López, L. Gasque and H. García-Ortega, *J. Mol. Struct.*, 2023, **1271**, 134009.
11 V. venkatarao, L. Kumar, A. Jha and G. Sridhar, *Chem. Data Collect.*, 2019, **22**, 100236.
12 R. Ustabaş, N. Süleymanoğlu, N. Özdemir, N. Kahriman, E. Bektaş and Y. Ünver, *Lett. Org. Chem.*, 2018, **17**, 46–53.
13 C. Tratrat, M. Haroun, I. Xenikakis, K. Liaras, E. Tsolaki, P. Eleftheriou, A. Petrou, B. Aldhubiab, M. Attimarad, K. N. Venugopala, S. Harsha, H. S. Elsewedy, A. Geronikaki and M. Soković, *Curr. Top. Med. Chem.*, 2019, **19**, 356–375.
14 L. V. Chinh, T. N. Hung, N. T. Nga, T. T. N. Hang, T. T. N. Mai and V. A. Tarasevich, *Russ. J. Org. Chem.*, 2014, **50**, 1767–1774.
15 M. Sökmen and M. Akram Khan, *Inflammopharmacology*, 2016, **24**, 81–86.
16 P. Yadav and K. Shah, *Bioorg. Chem.*, 2021, **109**, 104639.
17 Z. Muhammad, J. Yau, A. U. Zezi, M. G. Magaji, A. N. Hamza, Z. Muhammad, J. Yau, A. U. Zezi, M. G. Magaji and A. N. Hamza, *Am. J. Pharmacother. Pharm. Sci.*, 2023, **2**, 11.
18 H. O. Saxena, U. Faridi, J. K. Kumar, S. Luqman, M. P. Darokar, K. Shanker, C. S. Chanotiya, M. M. Gupta and A. S. Negi, *Steroids*, 2007, **72**, 892–900.
19 E. Polo, N. Ibarra-Arellano, L. Prent-Peñaloza, A. Morales-Bayuelo, J. Henao, A. Galdámez and M. Gutiérrez, *Bioorg. Chem.*, 2019, **90**, 103034.
20 E. Polo, J. Trilleras and M. G. Cabrera, *Molbank*, 2017, **2017**, M960.
21 O. V. Dolomanov, L. J. Bourhis, R. J. Gildea, J. A. K. Howard and H. Puschmann, *J. Appl. Crystallogr.*, 2009, **42**, 339–341.
22 G. M. Sheldrick, *Acta Crystallogr., Sect. C: Struct. Chem.*, 2015, **71**, 3–8.
23 Z. Chen, H. Duan, X. Tong, P. Hsu, L. Han, S. L. Morris-Natschke, S. Yang, W. Liu and K. H. Lee, *J. Nat. Prod.*, 2018, **81**, 465–474.
24 A. D. McLean and G. S. Chandler, *J. Chem. Phys.*, 1980, **72**, 5639–5648.
25 R. Krishnan, J. S. Binkley, R. Seeger and J. A. Pople, *J. Chem. Phys.*, 1980, **72**, 650–654.
26 Y. Zhao and D. G. Truhlar, *Theor. Chem. Acc.*, 2008, **120**, 215–241.
27 S. Miertuš, E. Scrocco and J. Tomasi, *Chem. Phys.*, 1981, **55**, 117–129.
28 M. E. Casida, C. Jamorski, K. C. Casida and D. R. Salahub, *J. Chem. Phys.*, 1998, **108**, 4439–4449.
29 J. L. Pascual-ahuir, E. Silla and I. Tuñon, *J. Comput. Chem.*, 1994, **15**, 1127–1138.
30 A. D. Becke, *J. Chem. Phys.*, 1993, **98**, 5648–5652.
31 C. Lee, W. Yang and R. G. Parr, *Phys. Rev. B: Condens. Matter Mater. Phys.*, 1988, **37**, 785–789.
32 W. J. Hehre, K. Ditchfield and J. A. Pople, *J. Chem. Phys.*, 1972, **56**, 2257–2261.
33 P. Geerlings, F. De Proft and W. Langenaeker, *Chem. Rev.*, 2003, **103**, 1793–1873.
34 P. J. Stephens, F. J. Devlin, C. F. Chabalowski and M. J. Frisch, *J. Phys. Chem.*, 1994, **98**, 11623–11627.
35 *CCCBDB listing of precalculated vibrational scaling factors*, **https://cccbdb.nist.gov/vibscalejustx.asp**, accessed 25 January 2024.
36 H. Chermette, *J. Comput. Chem.*, 1999, **20**, 129–154.
37 R. Dennington, T. A. Keith and J. M. Millam, *GaussView, Version 6.0*, Semichem Inc., Shawnee Mission, KS, 2016.
38 H.-B. Zhao, Y.-Q. Qiu, C.-G. Liu, S.-L. Sun, Y. Liu and R.-S. Wang, *J. Organomet. Chem.*, 2010, **695**, 2251–2257.
39 Y. Y. Hu, S. L. Sun, S. Muhammad, H. L. Xu and Z. M. Su, *J. Phys. Chem. C*, 2010, **114**, 19792–19798.
40 H. Abbas, M. Shkir and S. AlFaify, *Arabian J. Chem.*, 2019, **12**, 2336–2346.
41 E. Polo-Cuadrado, C. Rojas-Peña, K. Acosta-Quiroga, L. Camargo-Ayala, I. Brito, J. Cisterna, F. Moncada, J. Trilleras, Y. A. Rodríguez-Núñez and M. Gutierrez, *RSC Adv.*, 2022, **12**, 33032–33048.
42 M. Frimat, I. Boudhabhay and L. T. Roumenina, *Toxins*, 2019, **11**, 660.
43 E. Mathew and I. H. Joe, *J. Mol. Liq.*, 2023, **392**, 123415.
44 D. C. Harrowven, B. J. Sutton and S. Coulton, *Tetrahedron Lett.*, 2001, **42**, 2907–2910.
45 R. I. Al-Wabli, K. S. Resmi, Y. Sheena Mary, C. Yohannan Panicker, M. A. Attia, A. A. El-Emam and C. Van Alsenoy, *J. Mol. Struct.*, 2016, **1123**, 375–383.
46 S. Shettigar, P. Poornesh, G. Umesh, B. K. Sarojini, B. Narayana and K. Prakash Kamath, *Opt. Laser Technol.*, 2010, **42**, 1162–1166.